Supporting Information

Large single crystals of two-dimensional π-conjugated metal-organic frameworks via biphasic solution-solid growth

Dong-Gwang Ha, Mehdi Rezaee, Yimo Han, Saima A. Siddiqui, Robert W. Day, Lilia S. Xie, Brian J. Modtland, David A. Muller, Jing Kong, Philip Kim, Mircea Dincă* and Marc A. Baldo*

*Correspondence to: mdinca@mit.edu and baldo@mit.edu

This PDF file includes:

Materials and Methods

Materials

HHTP (95%), Nickel acetate (99.999%), Teflon coated magnets (TEF-D0050), 4-inch Si/SiO_2 wafers (Prime Grade, 285nm of dry chlorinated thermal oxide) were purchased from TCI America, Alfa Aesar, SuperMagnetMan, and Nova electronic materials, respectively.

Details of growth methods

The wafers were diced into half-inch by half-inch squares and twice cleaned by sonication in acetone for 2 minutes each, and in isopropyl alcohol (IPA) for 2 minutes, finished with soaking in boiling IPA for 5 minutes. HHTP was deposited onto the substrates by vacuum thermal evaporation at a rate of 0.3~2 Å/s at a pressure below 1×10^{-6} Torr. 10 mg of nickel acetate was dissolved in 4 mL of methanol and 10 μL of the solution was drop-cast onto the substrates 1~4 times. The two substrates were pressed together using Teflon coated magnets. The sandwiched substrates were immersed in 4~10 mL of water (purified with a Milli-Q system) in a 20-mL capacity vial. The vial was loosely capped and placed in a 95 °C oven. After the growth, the sample cooled down to room temperature naturally and the substrates were washed in water and dimethylformamide (DMF). The majority of the crystal plates remain on the HHTP substrate. No unexpected or unusually high safety hazards were encountered.

We did not find a clear correlation of growth outcome to the HHTP evaporation rate, deposition pressure, and amount of water within the given range. Patterning the HHTP film tends to help growth. When we employed a line pattern with 0.02-inch period, more crystals were grown on the substrate. We also tested the effect of magnetic force by reducing it by 50% or 80%, and could not find a clear correlation to the growth outcome. The magnetic forces were controlled by inserting two or four 1.1mm-thick glass substrates between the magnets, and we were able to grow planar crystals in all cases. We speculate that the tested magnetic forces marginally modulate the reaction space, which is a crucial factor to keep HHTP as a solid phase. We tested the growth at room temperature, and it did not generate the hexagonal crystals.

Typical growth conditions were a 40-nm-thick film of HHTP with the line pattern, drop-cast film of nickel acetate from 20 μL of 10 mM methanol solution, and 12-hour reaction time. With these conditions, micrometer-scale single-crystal plates were grown with high reproducibility. The growth condition occasionally gives large (over 10 μm) crystals, and the probability of getting large crystals increases by starting with thicker HHTP films. The diagonal of the plate-shaped crystals is 10 to 100 times bigger than their thickness. The thickness can be varied by adjusting the amount of reactants and reaction times as shown in Fig. S8.

Ellipsometery measurement

The measurement was performed on a J. A. Woollam M-2000 and confirmed with a J. A. Woollam WVASE32. Both instruments gave identical results. The sample was prepared by evaporation of a 30-nm-thick film of HHTP on a bare silicon substrate with a thin native oxide layer. The analysis started using the Cauchy model in the transparent region. Then it was slowly expanded to the whole region using the anisotropic B-spline model satisfying Kramers-Krönig consistency.

TEM sample preparation and measurement

A monolayer graphene grid (from Ted Pella Inc.) was used to minimize the charging effect of the crystals in a TEM. After the reaction was finished, we separated the two substrates which

were still wet with water. The water solution that contains the crystals was transferred to TEM grid and dried. An FEI Tecnai G2 spirit twin TEM was used for low-resolution imaging and quick sample screening. The TEM image shown in Fig. 3B was acquired in a Thermo Fisher Titan Themis at 120 keV. The conductive nature of the crystals and the supporting graphene layer contribute to less electron beam damages than other MOFs. The estimated electron dose rate for the high-resolution image was ~10^4 electrons/($Å^2 \cdot s$).

Optical band gap measurement

We determine the band gap based on the powder samples. We diluted the MOF powder at 1% in KBr and measured the diffuse reflectance for both FTIR (Bruker Tensor 37) and UV-vis-NIR (Agilent Cary 5000). Then the reflectance was converted to a Kubelka-Munk parameter which is proportional to the absorption coefficient over a scattering coefficient (*1*). The result is shown in Fig. S12A. To confirm the UV-Vis-NIR, we also measured the transmission. The transmission sample was prepared by dropcasting the MOF dispersed solution on a quartz substrate. To make the solution, we added methanol to the MOF powder and sonicated for one minute. The result is shown by the blue line in Fig. S12A. The trend matches the drift reflectance measurement. We used a Tauc plot to estimate the band gap as shown in Fig. S12B. Following the conventional protocol (*2–4*), we note the linear trend close to the band edge, which we extrapolate to yield an optical band gap of 0.18 eV.

FTIR measurement of single crystals

The crystals were transferred to a bare silicon substrate. Using an FTIR microscope (Bruker Lumos), we measured the transmittance of both the crystals and the silicon wafer. The spectrum is obtained by subtracting the background silicon signal.

Device fabrication with electron beam lithography

PMMA 950k C7 (from Microchem) was spun coat at 4000 rpm resulting in a ~1-μm-thick film. The substrate was baked at 180 °C for 1 minute. An Elionix ELS-F125 was used for electron beam lithography. The acceleration voltage, current, and dose were 125 kV, 1 nA, and 2000 C/$cm^{2,}$ respectively. After the exposure, it was developed in MIBK:IPA=1:3 solvent for 60 seconds and washed in IPA for 30 seconds. Ti/Au electrodes were deposited by vacuum thermal evaporation under ~1×10^{-6} Torr. The thickness was 300~400 nm.

Device fabrication with a stencil mask

The process starts with the fabrication of the stencil masks. The mask is based on a Si/Si_3N_4 (200nm) substrate. Multiple windows of 200μm×200μm squares are patterned by photolithography. For the largest patterns, 500μm×500μm squares were used. The silicon was etched to make a silicon nitride window. On the window, we used photolithography or electron beam lithography to make a desired pattern. Then, the silicon nitride was etched with a reactive ion etcher to finish the mask fabrication. To place the mask on the substrate, we applied a small amount of grease (Apiezon H) near the edge of the mask. Then the mask was placed on a desired position using a micropositioner. It is important to press the mask well to minimize the gap between the mask and the crystal. If the gap is too large, it will generate deposition shadows around the pattern that could short the device. Once the mask was well-positioned, we finished the device fabrication by evaporating metal. Gold and palladium contacts were tested, and the palladium electrode seems to provide a better electrical connection.

The pressed-pellet device fabrication

Ni-CAT-1 powders were pressed with 6.6 ton-force/cm^2. The pellet thicknesses were measured using a micrometer (Mitutoyo). The pellet was attached to a glass substrate with a grease (Apiezon N) and connected to gold wires with a carbon paste (Electron Microscopy Sciences Graphite Conductive Adhesive 112).

Electrical measurement

Conductivity was measured with a semiconductor parameter analyzer (Agilent 4156C) or a combination of a Keithley 2400 source meter and an Agilent 34401A multimeter with 10 GΩ input impedance. The temperature dependence was measured with an LN2-cooled cryo-probe station (Janis) or a He cryostat (Cryo Industries of America). For the Hall measurement, R_{xy} was obtained from the slope of current-voltage(I_{xx}-V_{xy}) measurement at each magnetic field. The magnetic field was swept both forward and reverse direction, and the data were averaged from 20 magnetic-field sweep measurements (10 forward and 10 reverse sweep measurements).

Supplementary Text

Crystal growth with different growth time

We varied the reaction time, and the growth results are shown in Fig. S2. After 30 minutes of growth, a few micrometer size plates are formed. Note that the surroundings of the crystals are HTTP film. This indicates that HHTP is not fully dissolved in water or reacted with nickel ions. After 1 hour of reaction, the formed crystal plates continuously grow or start to merge. The crystals are thicker than their surroundings, which means more HHTP molecules are consumed by dissolution to water or reaction with nickel ions. After 3 hours of reaction, the crystals are bigger due to merging and growth, but the crystal's edges and corners are still dull. Also, the crystal's color is not uniform, which indicates the irregular thickness of the plates. After 12 hours of reaction, the quality of the crystals is significantly improved. This indicates that the coordination bonding is reversible at the reaction temperature, and crystals can fix defects to minimize their energy.

Estimation of the gap between the two substrates

We placed a water droplet on the center of the Si/SiO_2 substrate and covered it with another substrate and pressed them with the two magnets. When the space between the substrates was smaller than a volume of the droplet, water was squeezed out. We systematically varied the droplet volume, and we estimated the reaction space is less than 1 μL which is equivalent to 6-μm gap. Additionally, the growth yield was lower when we placed 4-μm microspheres between the substrates. This suggests that the space is smaller than 4-μm gap. The minimum space is set by the flatness of the silicon substrates. The 4-inch silicon wafer has bow and warp less than 40 μm, and total thickness variation less than 10 μm. For the diced 0.5-inch substrates, we checked the flatness by 2D profile scan with a profilometer (Bruker DektakXT). As shown in Fig. S16, an average peak to valley value was 730 nm with the standard error of 130 nm. Therefore, the space can have a local gap of up to 1.5 μm solely from the substrate flatness.

Comments on the stacking structure of the MOF

The stacking structure of Ni-CAT-1 was suggested to have interpolated complexes between the MOF layers based on powder x-ray diffraction (PXRD) (*5*). In the same report, however, the high-resolution TEM images do not match the suggested structure, especially the metal element positions of the interlayer complexes. The authors speculate there may be a structural change upon activation or evacuation. More details of the TEM analysis is explained in ref. (*6*). Based on the discrepancy, Ni-CAT-1 might have two different stacking structures. This is not surprising considering the common observation of polymorphism in MOFs (*7*). Indeed, Cu-CAT-1 has two different stacking structures for different synthetic conditions (*8*, *9*). As the growth environment of the solution-solid growth is significantly different from the conventional hydrothermal method, the stacking structure might not be identical to the intercalated one. The reported simulated TEM images of Co-CAT-1 structure and its MOF layer are different as shown in Fig.1E of ref. (*5*) and Fig. 25 of ref. (*6*). The simulated Co-CAT-1 image has evident contrast between the triphenylene part and metal ions, whereas the MOF layer does not show the distinct contrast in the area. In the TEM image of Fig. 3, the contrast matches the latter implying a different stacking structure from Co-CAT-1. Further studies are required to identify the stacking sequence of the crystals.

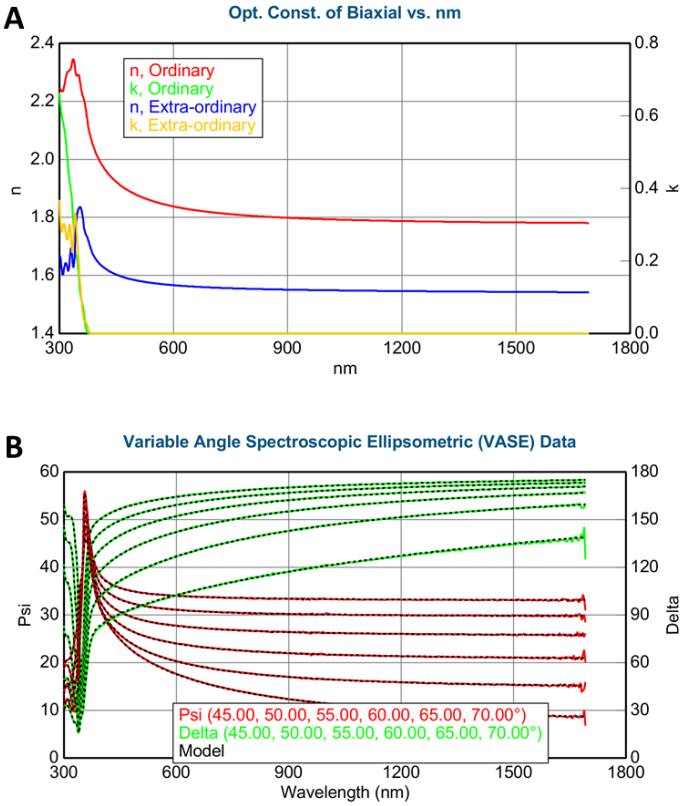

Fig. S1.

Ellipsometry data of an evaporated 34-nm-thick HHTP film on a silicon substrate. (A) Complex refractive indexes of ordinary and extraordinary direction. (B) Fitting results of Psi and Delta for variable angles.

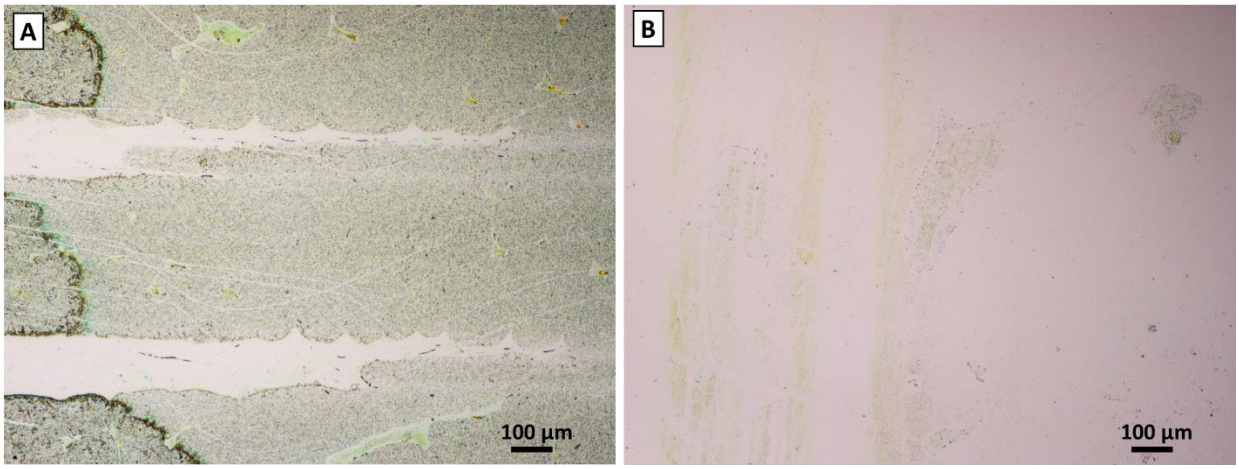

Fig. S2.

Optical microscope images of HHTP films after 1 hour (A) and 12 hours (B) under the typical growth condition except for the absence of nickel acetate. When we prepare the HHTP film, it is patterned with 0.01-inch stripe shape with a shadow mask. After 1 hour, the HHTP film remained solid, although some of the HHTP aggregates or dissolves. After 12 hours, the HHTP film is mostly dissolved in the water.

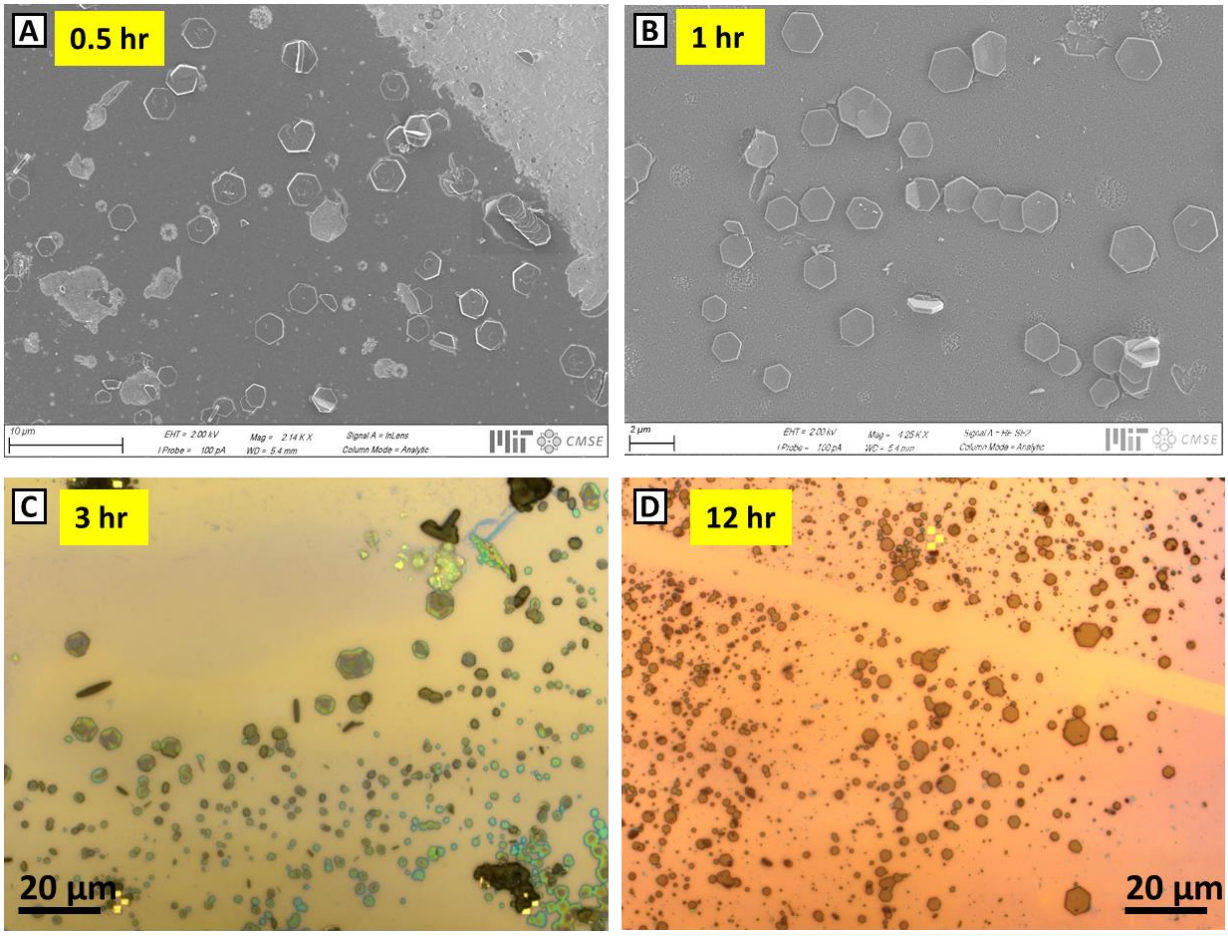

Fig. S3.

Growth results for different growth times. (A) half hour, (B) 1 hour, (C) 3 hours, (D) 12 hours of the reaction. Note that (A) and (B) are SEM images and (C) and (D) are optical microscope images. Also, the scale bars are different for the images.

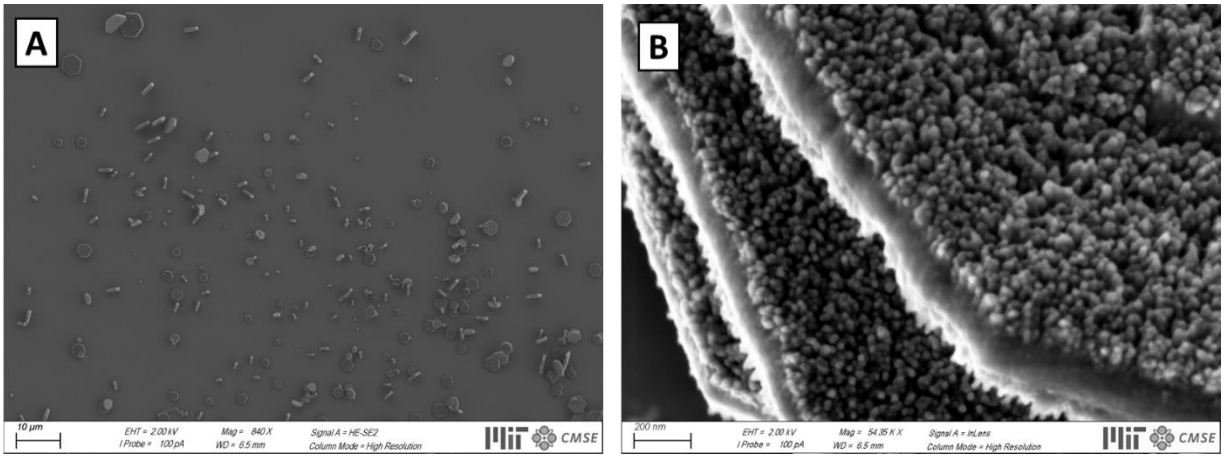

Fig. S4.

Growth with drop-cast HHTP film instead of an evaporated HHTP film. For the HHTP drop-casting, 10 µL of 1.7 mM methanol solution was drop-cast on a substrate two times. As shown in the low magnification image, the orientations of plates are random in contrast with crystals grown by evaporated HHTP. Even though plates have a hexagonal shape, they are composed of small grains. We speculate that small nanorod crystals are formed first and subsequently merged to form the plate shape. This might be related to the random orientation of HHTP molecules, which retards the basal plane growth. Also, the growth yield is low for the drop-cast HHTP. We obtained the above crystals from 4 independent trials whereas the evaporated HHTP film gives many micrometer-scale crystals from each run.

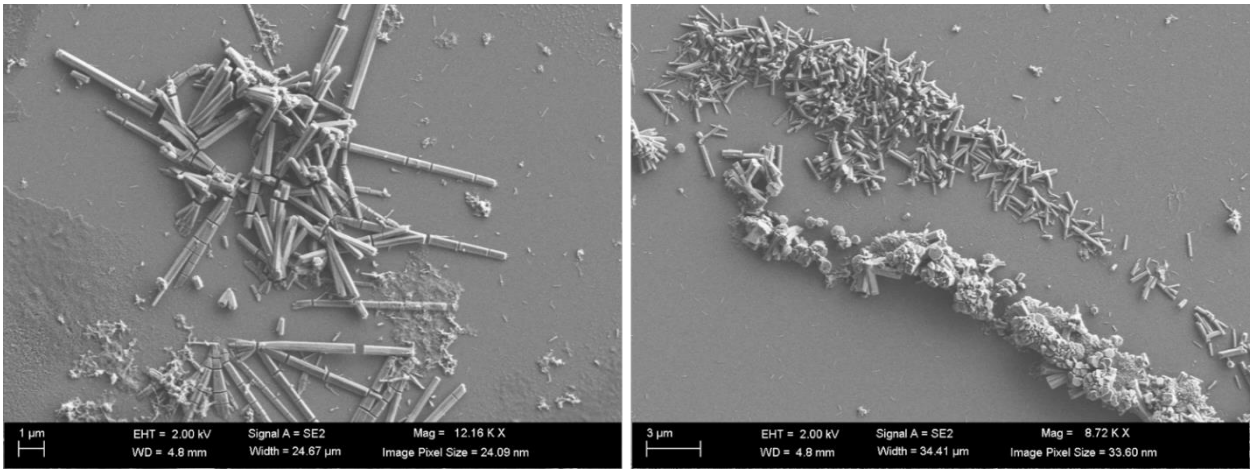

Fig. S5.

Growth with water-DMF(30%) cosolvent. HHTP is more than 500 times more soluble in DMF than water. Therefore, for growth with water-DMF(30%) cosolvent, the reaction occurred in a solution phase resulting in the rod-shape crystals. No crystal plates were observed.

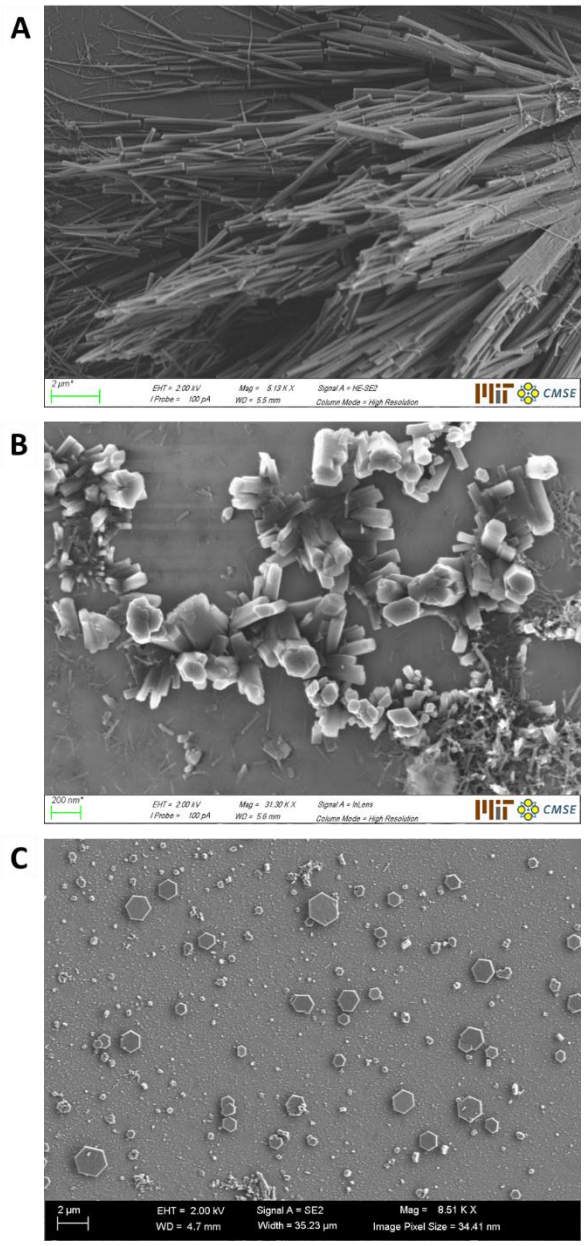

Fig. S6.

Control of the reaction space by dispersing different sizes of microspheres. (A) Growth with the 49-µm diameter microspheres. The gap resulted in very long crystals. Some of them exceed the aspect ratio of 500 and plate-shaped crystals were not found. Note that some of the wires are out-of-focus which indicates the tall heights of the wires, suggesting that they are grown from dissolved HHTP rather from a 40-nm-thick HHTP film. (B) Growth with 9-µm gap. It also generated wire- or cylinder-shaped crystals, and no plates were grown. (C) Growth with 4-µm gap. Some crystal plates were grown. The yield, size, and quality of the plates were low, indicating the space without the microspheres is smaller than the 4-µm gap.

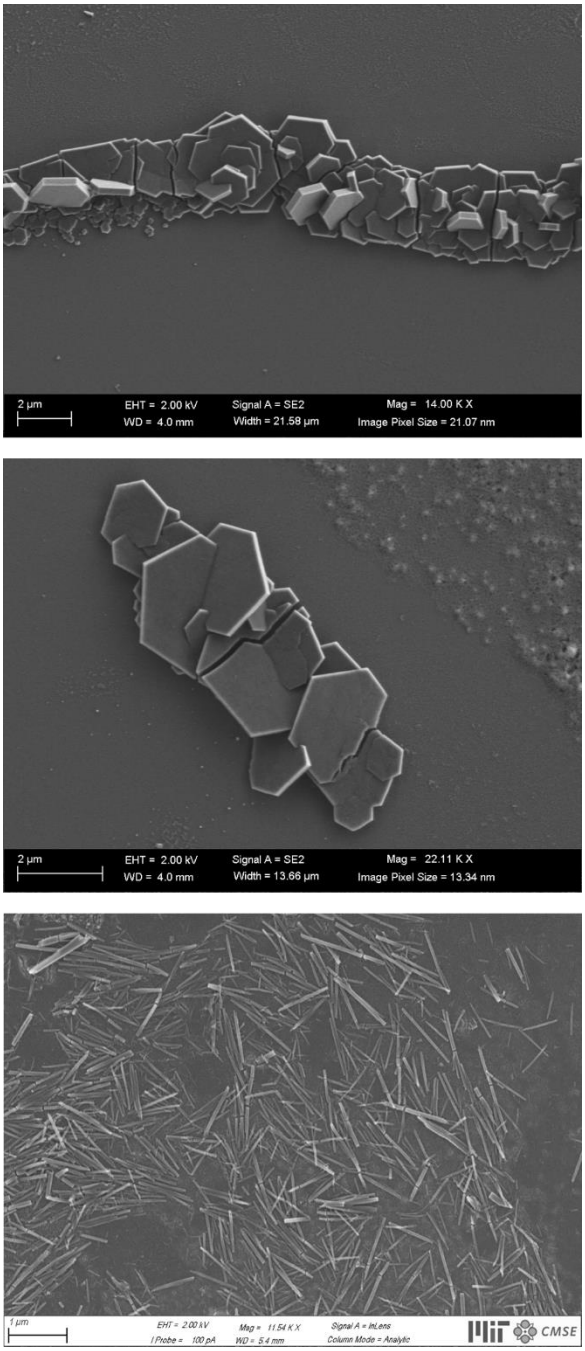

Fig. S7.

Polycrystalline or rod shape crystals of the MOF. We speculate that the local variation of nickel acetate concentration and dissolution of HHTP in water causes the different morphologies.

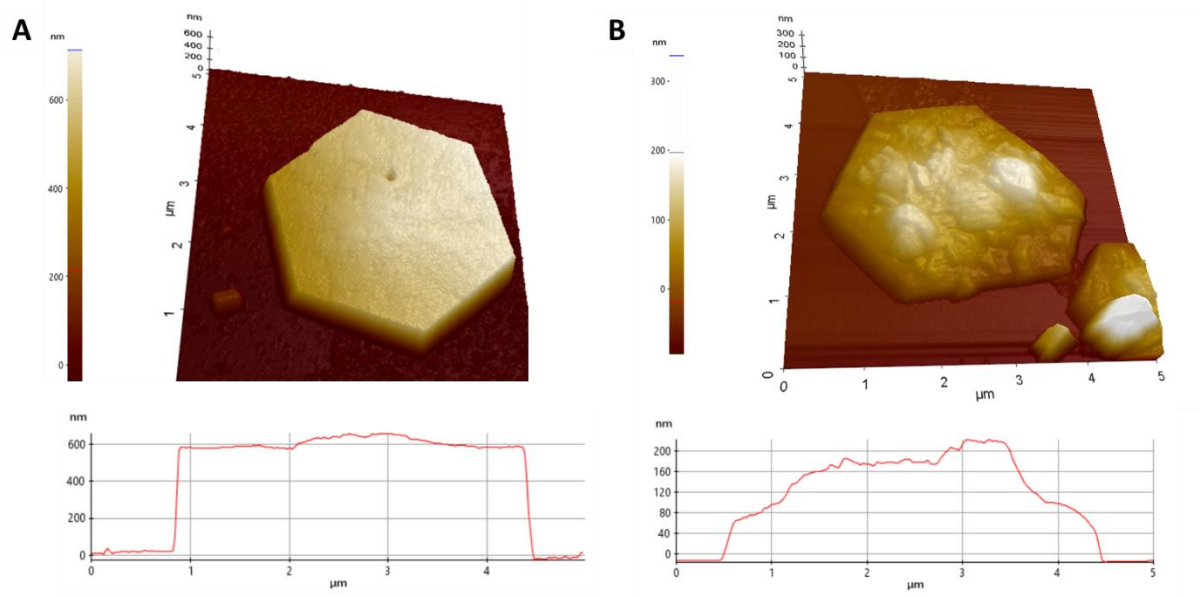

Fig. S8.

Atomic force microscope images of crystal plates for two different reaction conditions. The reaction times of A and B are 12 and 3 hours, respectively. Also, 5mg of sodium acetate was added for the growth of the crystals in B.

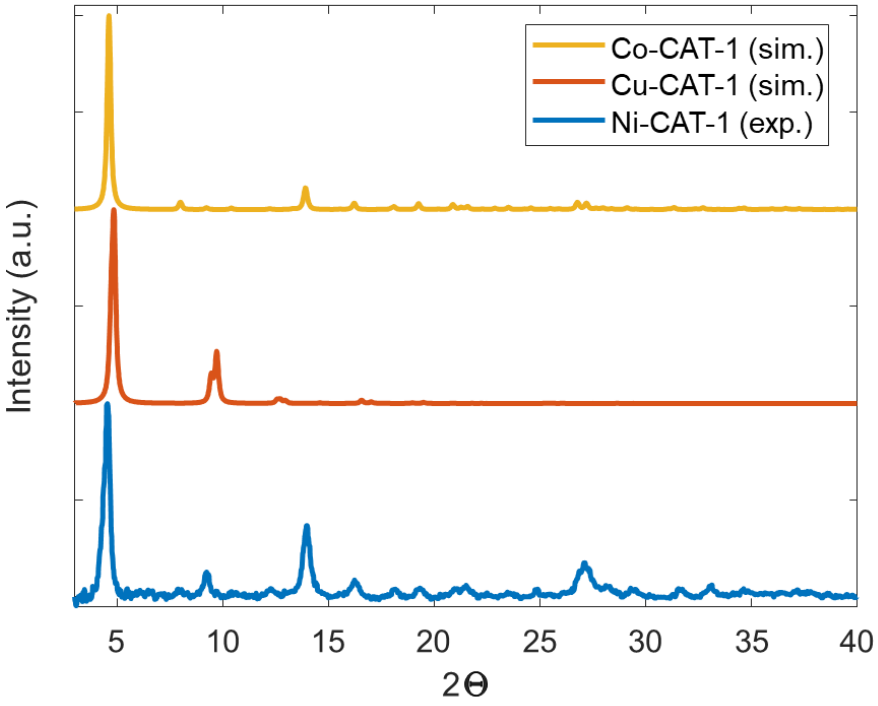

Fig. S9.

PXRD of Ni-CAT-1 powder synthesized by the reported hydrothermal method (*5*). The simulated patterns are generated from the single-crystal structure of Co-CAT-1 (*5*) and refined structure obtained from synchrotron PXRD of Cu-CAT-1 (*9*). The major peaks of Ni-CAT-1 match well with the simulated patterns of Co-CAT-1.

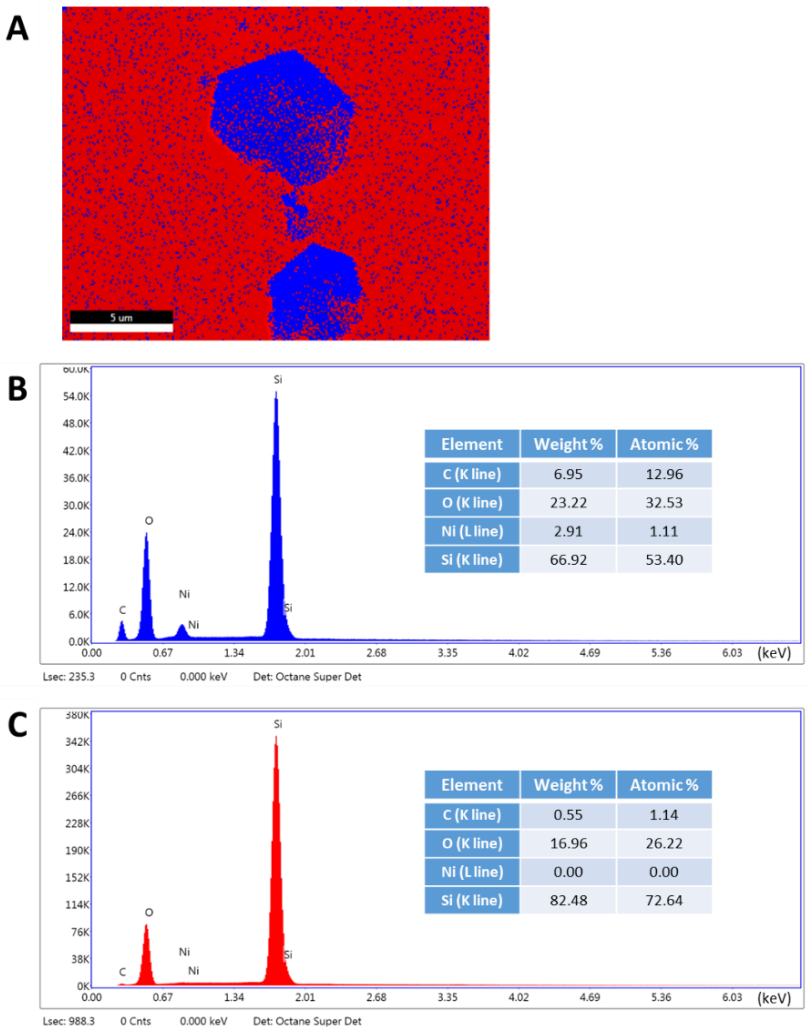

Fig. S10.

EDS analysis of Ni-CAT-1 crystals. (A) EDS phase mapping image. (B-C) EDS spectrum of the crystal (B) and background (C). The included tables are elemental analysis by eZAF quantification of EDAX TEAM software, and the tool is calibrated by an Al+Cu sample. The crystal (blue phase) has clear carbon and nickel peaks whereas the background (red phase) has only silicon and oxygen peaks.

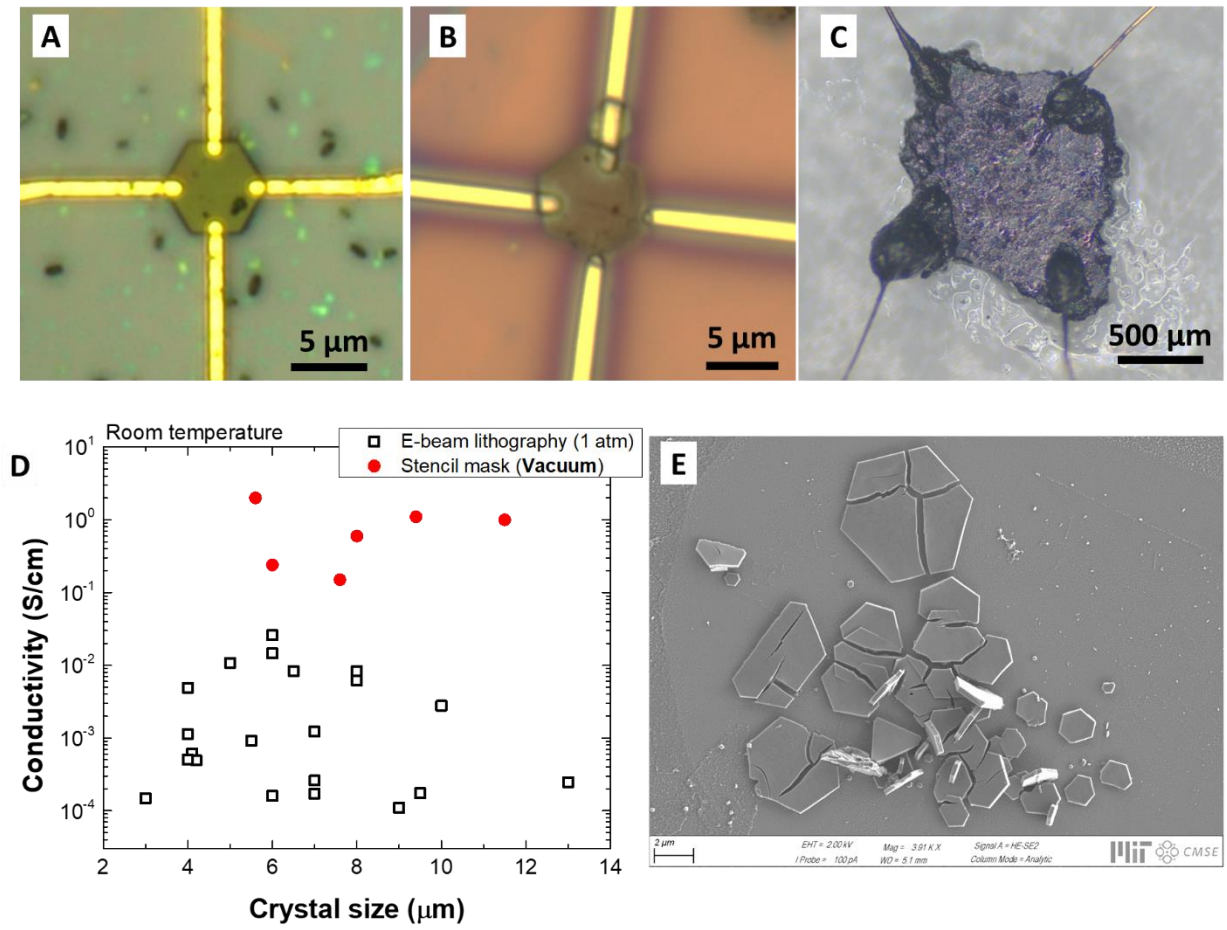

Fig. S11.

(A~C) Optical microscope images of fabricated devices. (A) A device made by electron beam lithography (B) A device fabricated with stencil mask technique. (C) A pressed-pellet device. (D) Electrical conductivities with various crystal sizes using the two fabrication methods. Note that the electrical conductivity increases by one order of magnitude under vacuum. All the devices fabricated with the stencil mask technique were measured under vacuum and the others were measured in an ambient environment. The electron beam lithography conditions were destructive to the crystals. The fabrication yield was about 50%, and the measured conductivity varies by two orders of magnitude for 21 samples. The stencil-mask samples show higher conductivity than electron beam samples and spread over one order of magnitude. Although the electron beam process was destructive, the best-measured conductivity of electron beam samples was similar to the stencil mask process. Therefore, further optimization of growth and fabrication parameters are required to use the electron beam lithography process. (E) An example of the single-crystal fracture after device fabrication with electron-beam lithography technique. Some crystals, especially bigger ones, tend to crack easier.

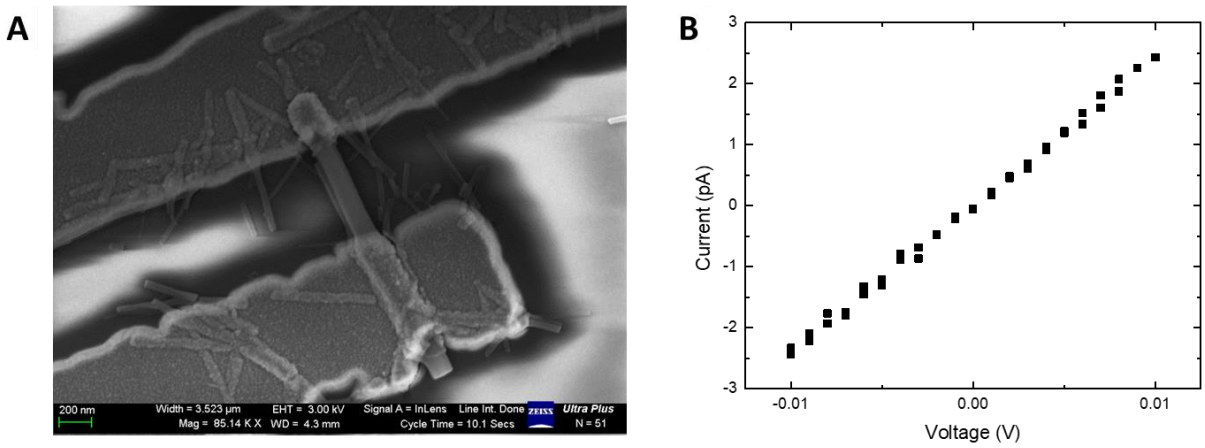

Fig. S12.

Out-of-plane (c-axis) conductivity of Ni-CAT-1. (A) Two probe device image (B) current-voltage curve. This gives a conductivity of 1×10^{-4} S/cm.

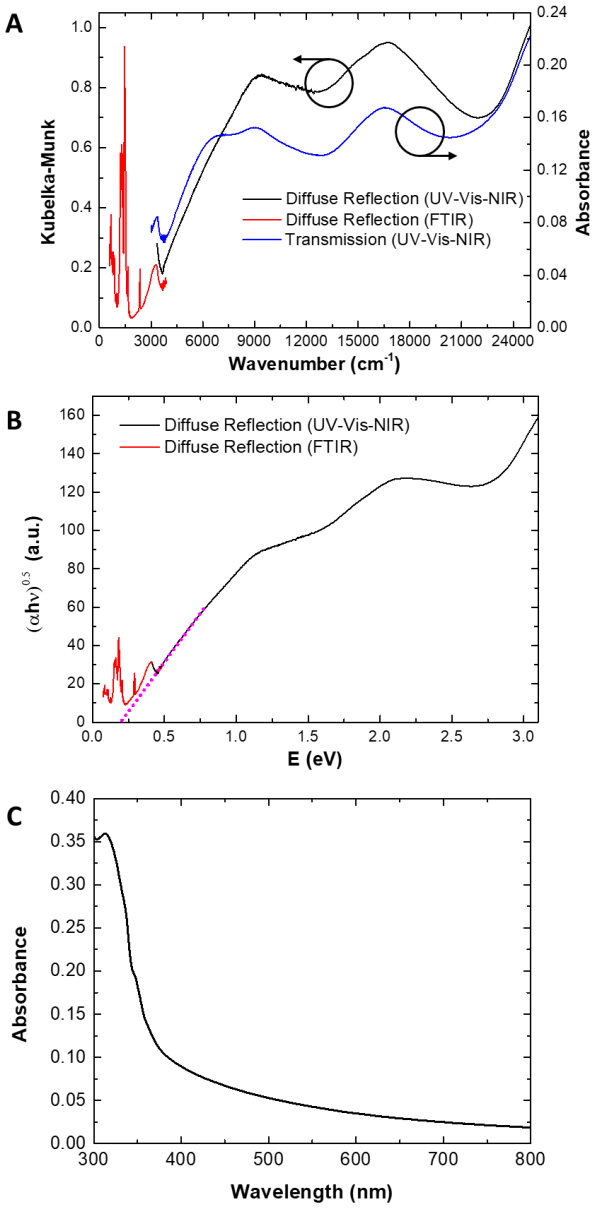

Fig. S13.

Band gap determination of $Ni_3(HHTP)_2$ powder (A) IR and UV-vis-NIR spectrum of $Ni_3(HHTP)_2$ powder by diffusive reflectance measurement (black and red) and transmission measurement (blue). (B) A Tauc plot with the indirect band assumption. The band gap is determined from the extrapolation of the linear band edge and it is 0.18 eV. (C) Absorbance of an evaporated HHTP film. The HOMO-LUMO gap is about 3.4 eV which is much bigger than the band gap of the MOF due to the π-conjugation. The continuous increase in the background at shorter wavelengths might originate from scattering caused by the wavelength-dependent variation in the refractive index of HHTP.

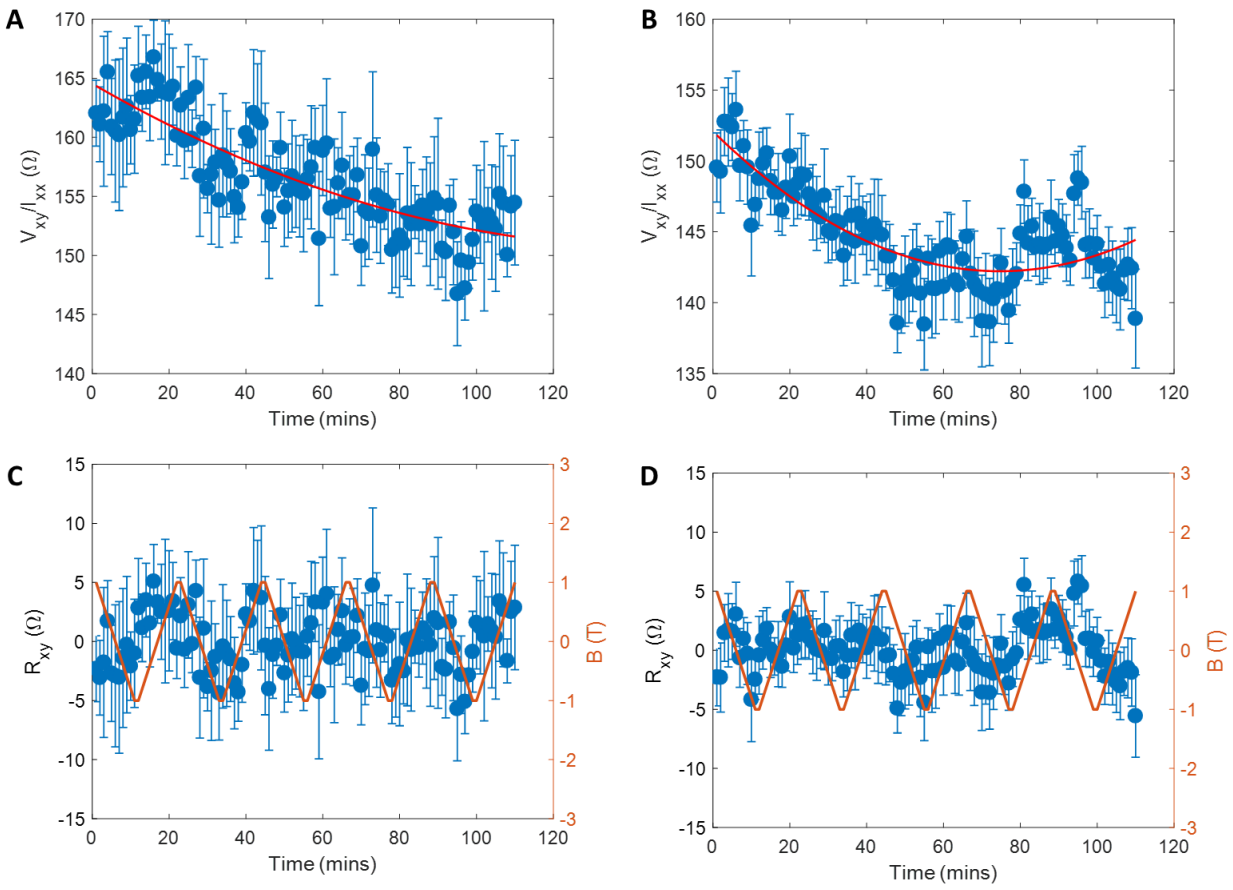

Fig. S14.

(A and B) Measured transverse resistance (V_{xy}/I_{xx}, where V_{xy} is transverse voltage and I_{xx} is longitudinal current) as a function of time. The transverse resistance should be zero in an ideal Hall geometry. In a real device, however, small misalignment of the electrodes is inevitable, resulting in a non-zero background resistance at zero magnetic field as shown above. It typically drifts over time and is independent of the magnetic field. The longitudinal current is swept from -1 to 1 μA for (A) and -4 to 4 μA for (B). Each point is the result of the current sweep. The red lines are quadratic fits. (C and D) Hall resistance (R_{xy}) is obtained from the difference between the transverse resistance and the fitting. The Hall resistances in (C) and (D) correspond to (A) and (B), respectively. Fig. 4G is an average of (C) and (D).

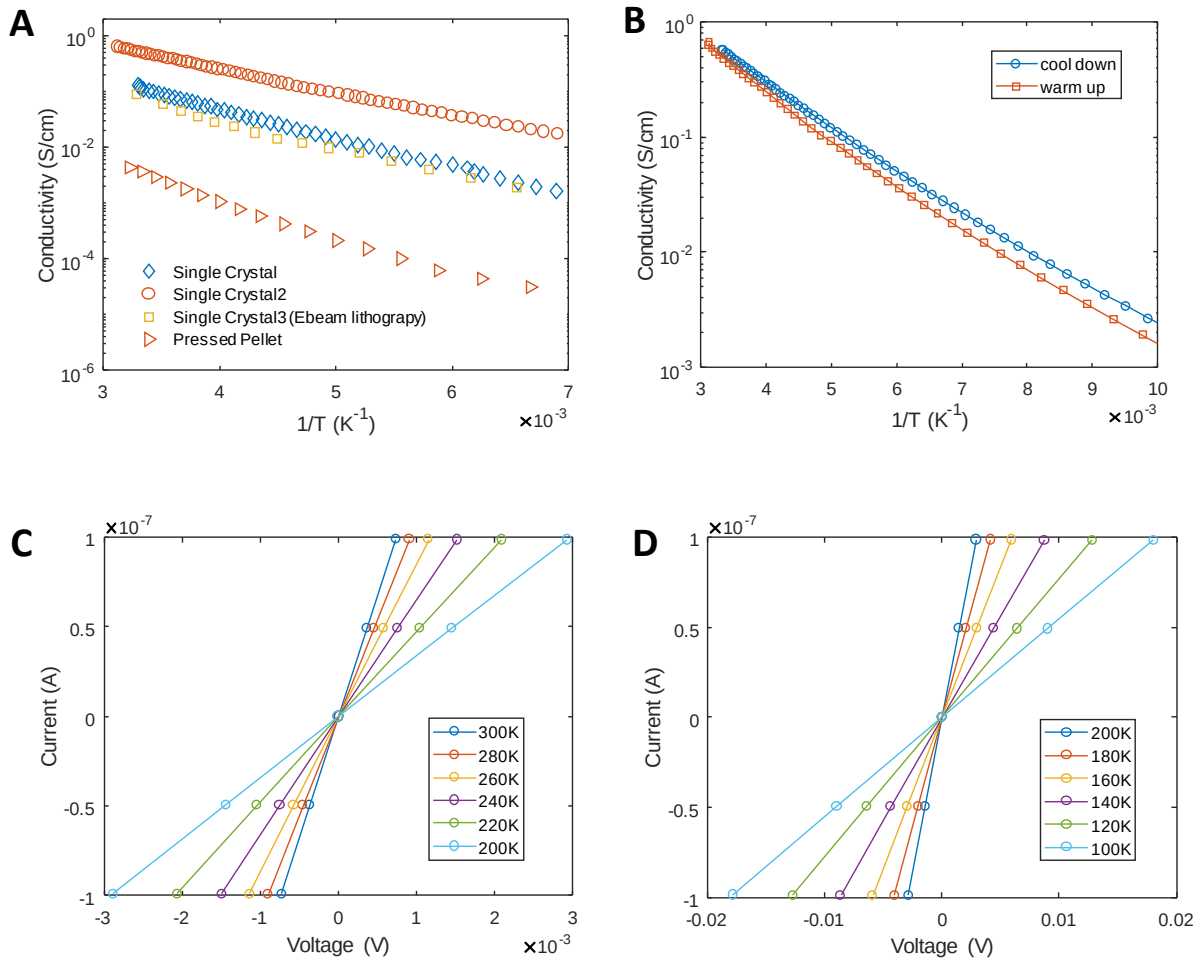

Fig. S15.

(A) Temperature dependence of electrical conductivities for three crystals. Crystal #3 is fabricated with electron beam lithography. (B) Typical cool-down and warm-up behavior of single-crystal conductivity. The cooling and heating rates are 4 K/min. (C and D) I-V characteristics at various temperatures.

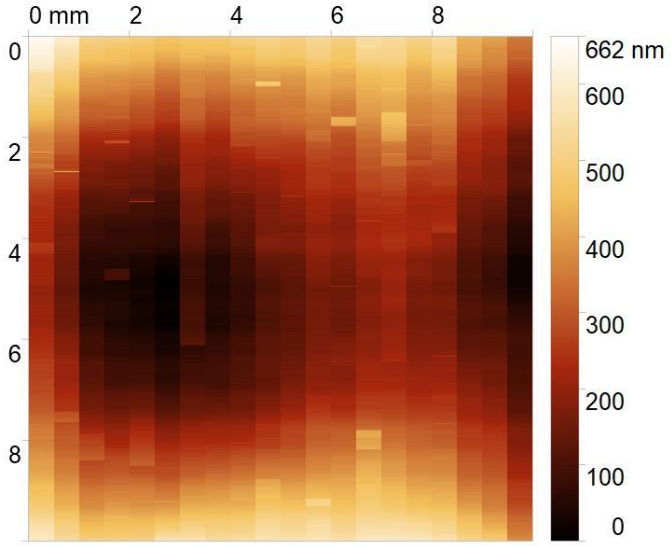

Fig. S16.

Surface profile of a 0.5-inch Si/SiO_2 substrate. The average peak to valley is 730 nm with a standard error of 130 nm.

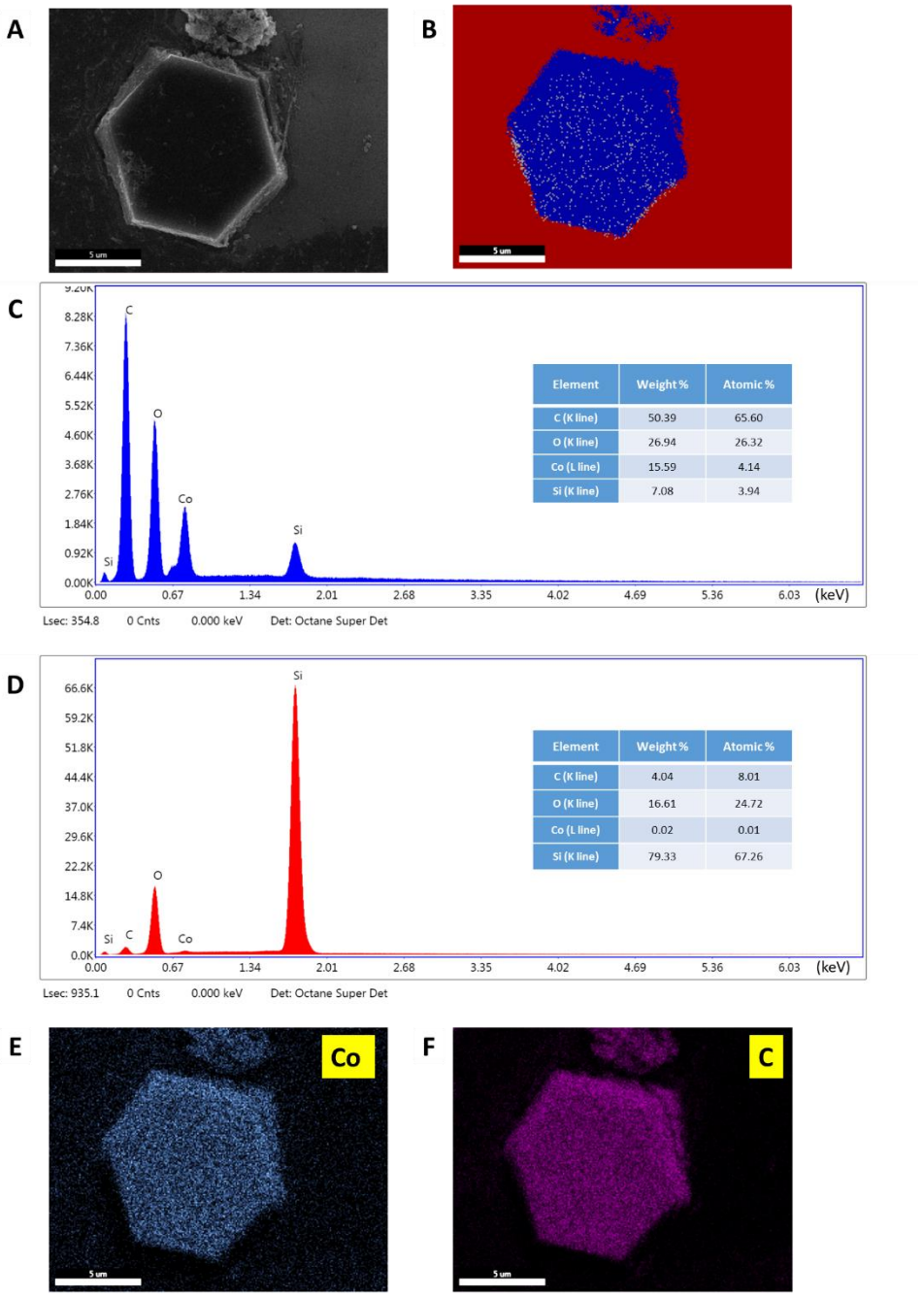

Fig. S17.

EDS analysis of a Co-CAT-1 single crystal grown by the solution-solid method. The growth condition was identical to the Ni-CAT-1 growth, except cobalt acetate was used instead of nickel acetate. (A) SEM image of Co-CAT-1 (B) Phase mapping image (C-D) EDS spectrum of the crystal (blue phase) and background (red phase). The included tables are elemental analysis. (E-F) Elemental mapping of cobalt (E) and carbon (E).

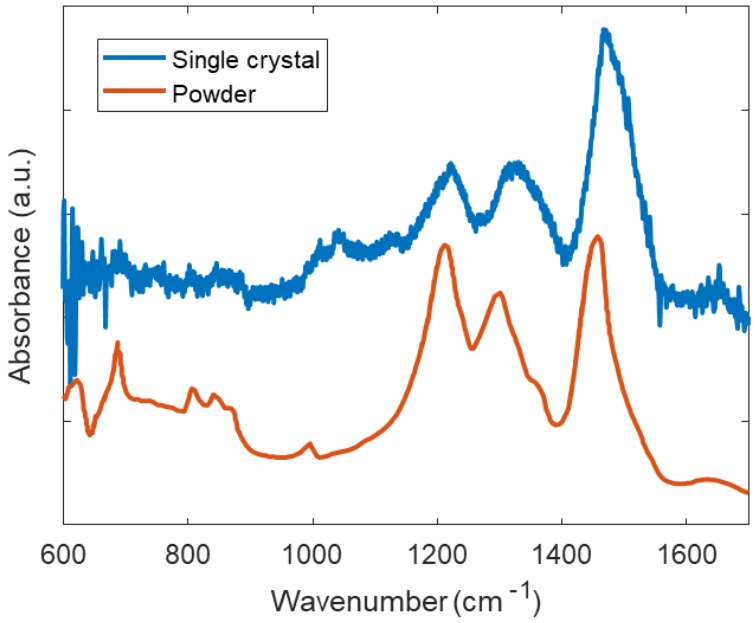

Fig. S18.

FT-IR spectrum of a Co-CAT-1 single crystal and powder. The vibrational features of the crystal and powder are similar. The powder was synthesized following the ref. (*5*) and confirmed by PXRD.

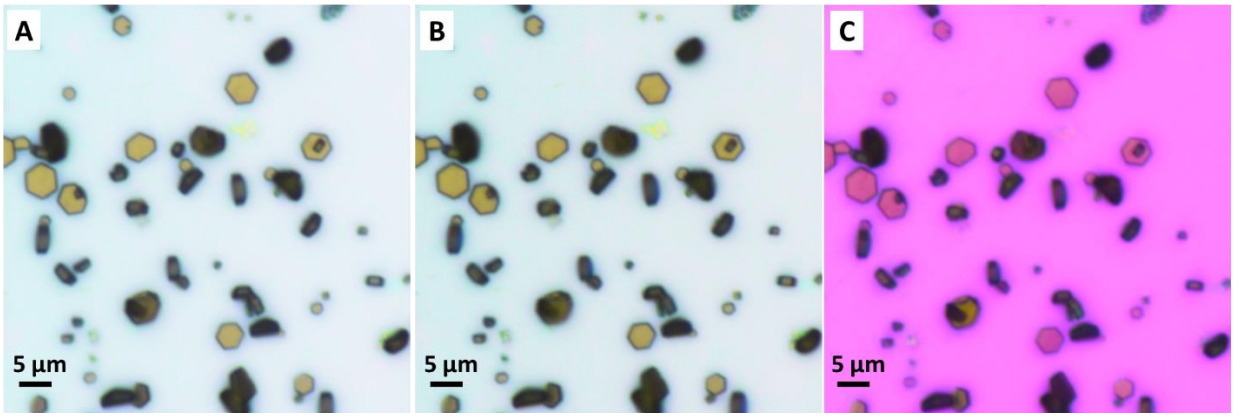

Fig. S19.

Polarized light microscope images. No-polarized (A), plane-polarized (B), cross-polarized (C) images were taken with Nikon Eclipse LV150NA. In addition to the clear hexagonal shape and TEM analysis, the polarized images support the single crystallinity of the crystals.

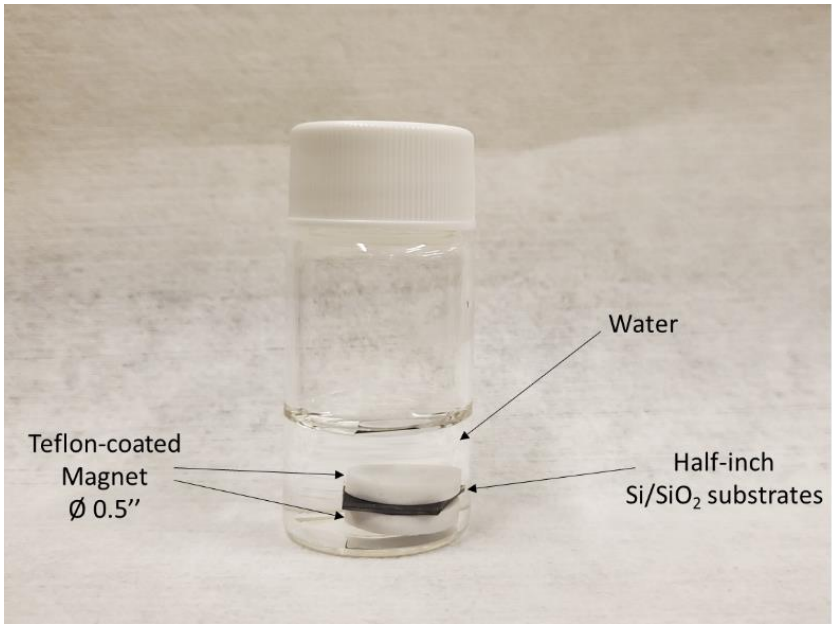

Fig. S20.
A photograph of the growth chamber described in Fig. 1C.

Table S1.

Comparison of the carrier mobility and carrier density values with other materials. Hall mobility data are preferentially selected because of overestimation issues in field-effect transistor measurement (*10*).

Materials		σ [a] (S/cm)	μ [b] ($cm^2 \cdot V^{-1} \cdot s^{-1}$)	n [c] (cm^{-3})	Morphology	Carrier type	Measurement method	Ref.
MOFs	Ni-CAT-1	0.4	0.16	1.4×10^{19}	Single crystal (Basal plane)	e^-	Hall	This work
	$Fe_3(THT)_2(NH_4)_3$	0.034	229	9.2×10^{14}	Polycrystalline (thin film)	h^+	Hall	(*11*)
	$Ni_3(HITP)_2$	.	49	.	Polycrystalline (thin film)	h^+	Field-effect transistor	(*12*)
Small molecule	Rubrene	7.2×10^{-8}	10	4.5×10^{14}	Single crystal	h^+	Hall	(*13*)
	Rubrene	.	0.002	.	Polycrystalline (thin film)	h^+	Field-effect transistor	(*14*)
2D materials	MoS_2	.	10	1×10^{13} [d]	Single crystal	e^-	Hall	(*15*)
	Black phosphorus	.	1	7.0×10^{12} [d]	Single crystal	h^+	Hall	(*16*)
Silicon (Doping: 10^{18} cm^{-3})		1.6	100	1×10^{18}	Single crystal	h^+	Hall	(*17*)
Silicon (Doping: 10^{18} cm^{-3})		1.6×10^{-4}	1	1×10^{16}	Polycrystalline (thin film)	h^+	Hall	
Silicon (Doping: 10^{16} cm^{-3})		0.48	300	1×10^{16}	Single crystal	h^+	Hall	
Silicon (Doping: 10^{16} cm^{-3})		4.8×10^{-6}	30	1×10^{11}	Polycrystalline (thin film)	h^+	Hall	
Copper		6.0×10^{5}	33	1.1×10^{23}	Polycrystalline (thin film)	e^-	Hall	(*18*)
Gold		3.6×10^{5}	25	8.9×10^{22}	Polycrystalline (thin film)	e^-	Hall	

[a] Electrical conductivity, [b] Mobility, [c] Carrier density, [d] Areal carrier density. The unit is cm^{-2}.

Table S2.

Crystal growth yield under the typical growth conditions described in the method section. Crystal counting was performed manually with an optical microscope.

Crystal size (μm)	Average #	Standard deviation
4~6	20	7.8
6~8	4.0	1.9
8~10	1.4	1.3
>10	0.6	0.9

References

1. P. Kubelka, F. Munk, Ein Beitrag zur Optik der Farbanstriche. *Zeits. f. Techn. Phys.* **12**, 593 (1931).
2. J. Tauc, OPTICAL PROPERTIES AND ELECTRONIC STRUCTURE OF AMORPHOUS Ge AND Si. *Mater. Res. Bull.* **3**, 37 (1968).
3. D. G. Barton, M. Shtein, R. D. Wilson, S. L. Soled, E. Iglesia, Structure and Electronic Properties of Solid Acids Based on Tungsten Oxide Nanostructures. *J. Phys. Chem. B.* **103**, 630–640 (1999).
4. N. E. Thornburg, Y. Liu, P. Li, J. T. Hupp, O. K. Farha, J. M. Notestein, MOFs and their grafted analogues: Regioselective epoxide ring-opening with Zr6 nodes. *Catal. Sci. Technol.* **6**, 6480–6484 (2016).
5. M. Hmadeh, Z. Lu, Z. Liu, F. Gándara, H. Furukawa, S. Wan, V. Augustyn, R. Chang, L. Liao, F. Zhou, E. Perre, V. Ozolins, K. Suenaga, X. Duan, B. Dunn, Y. Yamamto, O. Terasaki, O. M. Yaghi, New Porous Crystals of Extended Metal-Catecholates. *Chem. Mater.* **24**, 3511–3513 (2012).
6. Z. Liu, N. Fujita, K. Miyasaka, L. Han, S. M. Stevens, M. Suga, S. Asahina, B. Slater, C. Xiao, Y. Sakamoto, M. W. Anderson, R. Ryoo, O. Terasaki, A review of fine structures of nanoporous materials as evidenced by microscopic methods. *J. Electron Microsc. (Tokyo).* **62**, 109–146 (2013).
7. A. Karmakar, A. Paul, A. J. L. Pombeiro, Recent advances on supramolecular isomerism in metal organic frameworks. *CrystEngComm*. **19**, 4666–4695 (2017).
8. V. Rubio-Giménez, M. Galbiati, J. Castells-Gil, N. Almora-Barrios, J. Navarro-Sánchez, G. Escorcia-Ariza, M. Mattera, T. Arnold, J. Rawle, S. Tatay, E. Coronado, C. Martí-Gastaldo, Bottom-Up Fabrication of Semiconductive Metal–Organic Framework Ultrathin Films. *Adv. Mater.* **30**, 1–8 (2018).
9. R. W. Day, D. K. Bediako, M. Rezaee, L. R. Parent, G. Skorupskii, M. Q. Arguilla, C. H. Hendon, I. Stassen, N. C. Gianneschi, P. Kim, M. Dincă, Single Crystals of Electrically Conductive Two-Dimensional Metal-Organic Frameworks: Structural and Electrical Transport Properties. *ACS Cent. Sci.* **5**, 1959–1964 (2019).
10. H. H. Choi, K. Cho, C. D. Frisbie, H. Sirringhaus, V. Podzorov, Critical assessment of charge mobility extraction in FETs. *Nat. Mater.* **17**, 2–7 (2017).
11. R. Dong, P. Han, H. Arora, M. Ballabio, M. Karakus, Z. Zhang, C. Shekhar, P. Adler, P. S. Petkov, A. Erbe, S. C. B. Mannsfeld, C. Felser, T. Heine, M. Bonn, X. Feng, E. Cánovas, High-mobility band-like charge transport in a semiconducting two-dimensional metal–organic framework. *Nat. Mater.* **17**, 1027–1032 (2018).
12. G. Wu, J. Huang, Y. Zang, J. He, G. Xu, Porous field-effect transistors based on a semiconductive metal-organic framework. *J. Am. Chem. Soc.* **139**, 1360–1363 (2017).
13. V. Podzorov, E. Menard, J. A. Rogers, M. E. Gershenson, Hall effect in the accumulation layers on the surface of organic semiconductors. *Phys. Rev. Lett.* **95**, 1–4 (2005).
14. S. W. Park, S. H. Jeong, J. M. Choi, J. M. Hwang, J. H. Kim, S. Im, Rubrene polycrystalline transistor channel achieved through in situ vacuum annealing. *Appl. Phys. Lett.* **91**, 1–4 (2007).
15. B. Radisavljevic, A. Kis, Mobility engineering and a metal-insulator transition in monolayer MoS 2. *Nat. Mater.* **12**, 815–820 (2013).
16. L. Li, F. Yang, G. J. Ye, Z. Zhang, Z. Zhu, W. Lou, X. Zhou, L. Li, K. Watanabe, T. Taniguchi, K. Chang, Y. Wang, X. H. Chen, Y. Zhang, Quantum Hall effect in black

phosphorus two-dimensional electron system. *Nat. Nanotechnol.* **11**, 593–597 (2016).
17. J. Y. W. Seto, The electrical properties of polycrystalline silicon films. *J. Appl. Phys.* **46**, 5247–5254 (1975).
18. K. L. Chopra, S. K. Bahl, Hall effect in thin metal films. *J. Appl. Phys.* **38**, 3607–3610 (1967).